

Low-Profile Embedded Hybrid Terrestrial/Nonterrestrial 5G Antenna for Automotive Applications

Umair Tayyab, Muhammad Ehtisham Asghar, Tristan Koppe, Hans-Peter Petry, Thomas Wack, and Matthias A. Hein

Abstract – Low-earth orbit satellite constellations serving 5G mobile communications offer seamless wireless connectivity, particularly suited for automated and connected vehicles. Low-profile user equipment antenna terminals that support both terrestrial and nonterrestrial communications are essential for addressing automotive mass-market applications. This letter introduces a hybrid 3-in-1 automotive antenna that operates at 2.6 GHz for terrestrial links in the 5G new-radio (NR) band n41, at 3.5 GHz for both terrestrial and nonterrestrial networks targeting the 5G NR band n78, and at 28 GHz for satellite links in the n257-band. This shared-aperture antenna design is suitable for embedding into plastic exterior parts of car bodies. For terrestrial connectivity, a linearly polarized quadripod kettle antenna, made of metalized plastics, revealed an omnidirectional horizontal radiation pattern at the bands n41 and n78 with realized gains of 6 dBi and 5.6 dBi, respectively. For nonterrestrial communications, nested circularly polarized microstrip slot patch arrays provided dual-band connectivity in the S-band (3.5 GHz) and Ka-band (28 GHz), achieving realized gains of 6.3 dBi and 11 dBi along the broadside direction toward the zenith. Anticipating further improved decoupling, feeding, and embedding paves the way toward viable applications.

1. Introduction

The potential of 5G mobile communication technology is not limited to providing higher data rates or lower latencies compared with preceding standards but also offers a combination of terrestrial (TN) and nonterrestrial communication networks (NTN). A major advantage of 5G nonterrestrial links to very-low-earth orbit (VLEO) satellite constellations is the improvement of coverage and availability on roads and rails, especially in shadowed

urban regions or underserved rural areas, by complementing terrestrial links. Potential applications particularly address highly automated systems for the transportation of passengers or goods, for which seamless connectivity presents a key prerequisite [1].

VLEO satellite communications with orbital heights of $d = 100 - 450$ km enable seamless wireless coverage with lower path loss, lower transmission latencies, and correspondingly higher data rates compared with higher-orbit satellite constellations. To achieve true broadband connectivity, different spectral ranges were selected to enable 5G communication links compliant with 3GPP standards [2]. The S-band is considered feasible for 5G TN/NTN applications in downlink and uplink due to its lower terminal costs, attractive link budget and data rates, and chipset availability, while the Ka-band offers broader absolute bandwidths and smaller antenna dimensions, attractive for downlink. The accessibility of high-gain satellite antennas in VLEO constellations unlocks the potential of using low-profile user terminal antennas with moderate gain and without the need for beam-steering capability. A major practical benefit is the resulting suitability of such terminals for low-cost, conformal plastic-embedded mounting into slim exterior parts of car bodies [2, 3], which opens up a mass market for automotive applications [4].

This contribution presents a hybrid 3-in-1 antenna terminal operating in the n78 band (3.3 – 3.8 GHz) for both TN/NTN and, at the same time, in the n41 band (2.5 – 2.7 GHz) for TN and in the n257 band (26.5 – 29.5 GHz) for NTN. The bands cover both uplink and downlink frequencies according to 3GPP [5]. The dual-band circularly polarized NTN antenna is a combination of a 2×2 aperture-coupled patch array for the n78 band and a 4×4 single-layer patch array for the n257 band. A 3D linearly polarized quadripod kettle antenna (QKA) covering the bands n41 and n78 was designed for TN and manufactured from metalized plastics. All radiating elements are integrated into a single platform, well suited for embedded mounting into, for example, the rear spoiler of a car. Section 2 outlines the antenna requirements derived from the link budget. Section 3 describes the proposed user equipment terminal. The results of numerical simulations and measurements are summarized in Section 4, followed by conclusions in Section 5.

2. Antenna Performance Requirements

VLEO constellations employing high-gain satellite antennas and offering direct-to-vehicle connectivity

Manuscript received 9 December 2024. This research was funded by the German Space administration (DLR) under the grant 50 RK 2121.

Umair Tayyab and Muhammad Ehtisham Asghar are with the RF & Microwave Research Group, Thuringian Center of Innovation in Mobility, Technische Universität Ilmenau, Germany; umair.tayyab@tu-ilmenau.de, ehtisham.asghar@tu-ilmenau.de.

Tristan Koppe and Thomas Wack are with Wiegand GmbH, OT Schlotheim, Germany; tristan.koppe@wiegand-tec.de, thomas.wack@wiegand-tec.de.

Hans-Peter Petry is with the German Center for Satellite Communications (DeSK), Backnang, Germany; petry.hp@t-online.de.

Matthias A. Hein is with the RF & Microwave Research Group, Thuringian Center of Innovation in Mobility, Technische Universität Ilmenau, Germany; matthias.hein@tu-ilmenau.de.

enable broadband 5G mobile communications with medium-gain fixed-beam ground terminal antennas. As beam-steering capability may become obsolete for such constellations, the costs and complexity of the user equipment terminal can be significantly reduced compared with approaches that necessitate phased arrays. Realistic link budgets were analyzed for such constellations for the n78 and n257 bands in [6–8]. An uplink (UL) data rate of $DR_{UL} = 21$ Mbit/s at $f = 3.5$ GHz was anticipated for an antenna gain of $G_{NTN} = 10$ dBi, and a UL data rate of $DR_{UL} = 7$ Mbit/s at $f = 28$ GHz was calculated for a gain of $G_{NTN} = 15$ dBi. Such gain values can be realized with antenna dimensions as small as 2.5λ , depending on the achievable radiation and matching efficiencies, where λ denotes the free-space wavelength. Referring to the data rates above, automotive consortia, like the 5GAA, identified numerous relevant use cases where data rates of this order could be beneficially used [4, 9]. For instance, the “obstructed view assist” provides a host vehicle with an alternate view of the obstructed road segment, requiring $DR = 5$ Mbit/s and a transmission latency of $L = 50$ ms; disengagement reports by host vehicles to government data centers necessitate a data rate $DR > 25$ Mbit/s, with no critical latency requirement. TN could cover applications requiring higher data rates, lower latencies, or require larger antenna apertures.

Additional performance parameters must be considered when designing a hybrid 3-in-1 antenna. According to 3GPP, NTN antennas should cover at least bandwidths of $B_{op} = 100$ MHz and 400 MHz at the n78 and n257 bands around the center frequencies $f = 3.5$ GHz and $f = 28$ GHz, respectively, while $B_{op} = 20$ MHz would be required for TN antennas [10]. In terms of polarization purity, an axial ratio $AR < 3$ dB and a cross-polar discrimination $XPD > 15$ dB are considered suitable for NTN and TN antennas, respectively, over the respective bandwidths [11]. Eventually, the angular width $\Delta\Theta$ and direction Θ_0 of the main beam must be considered appropriately so that the resulting field-of-view is covered with adequate gain. Our goal was to achieve $\Delta\Theta_{NTN} = \pm 30^\circ$ around $\Theta_0 = 90^\circ$ with $G_{NTN} = 10 - 15$ dBi as attractive target values for efficient 5G automotive satellite communications. The TN antenna should have an omnidirectional radiation pattern $\Delta\Theta_{TN} = 60^\circ - 90^\circ$ with a nominal gain value of $G_{TN} \approx 3$ dBi or better.

3. Hybrid 3-in-1 Antenna Design

One major incentive to use a quadripod kettle antenna for automotive applications is its feasibility for combination with the patch-based NTN radiators while displaying an omnidirectional horizontal gain pattern with a low profile. In an initial design phase, a QKA made from brass sheath material was developed and successfully tested [3]. As a further step toward design for manufacturability, another QKA version was fabricated from acrylonitrile butadiene styrene coated with copper, with a sheet thickness of 35 μm . Measurements of the radiation pattern, gain, and

directivity values revealed identical performance for both versions. As visualized in Figure 1a, the QKA was placed at the center of the dual-band nested multilayer NTN arrays described in [2], sharing the same ground plane as the 2×2 -elements 3.5-GHz array. Differing from the previous arrangement, the 4×4 -elements 28-GHz array was attached to the top square of the QKA with double-sided conductive adhesive, maintaining the fourfold rotational symmetry on the printed circuit board, according to Figure 1b. The aerial footprint of the resulting hybrid 3-in-1 antenna measured 93×93 mm, with a height of 15 mm. The QKA was centrally fed via a coaxial cable equipped with an SMA connector, whose flange was soldered to the bottom of the ground plate. To feed the 3.5-GHz array, a 50- Ω microstrip transmission line was connected vertically at the edge of the printed circuit board. For the 28-GHz array, the center of the 50- Ω microstrip feed line on the bottom side contained through-holes to connect to an RF coaxial cable extending below the 3.5-GHz array. The complete antenna was embedded into a commercially available rear spoiler of a passenger sport utility vehicle (here: Skoda Kodiaq) to examine the influence of plastic embedding on the antenna performance.

For testing in the rear spoiler, the antenna board was mounted near one corner of the rear spoiler, as depicted in Figure 1c. The printed circuit board was fully covered by acrylonitrile butadiene styrene, with a dielectric permittivity of $\epsilon_r = 2.6$ and a loss tangent of $\tan \delta = 0.0169$ at 8.2 GHz [12]. The low-profile antenna with a height of $h = 15$ mm could be easily embedded into the rear spoiler, given its larger height of 40 mm. Furthermore, mounting the radiator in the rear spoiler provides the advantage of aligning the different fields of view for the TN and NTN radiators. In a later development step, the 3-in-1 antenna terminal in the rear spoiler was then integrated into a car.

4. Simulation and Measurement Results

The bare version of the 3-in-1 antenna (i.e., visible to the environment) was designed using electromagnetic full-wave simulations with CST Studio Suite 2024 [13]. The measurements were carried out in a shielded anechoic chamber with a ± 1 -dB measurement uncertainty across the frequency ranges of interest, as illustrated in Figure 2a. The antenna was mounted on a lightweight plastic holder and bolted to the rotating metallic positioner, which was covered with pyramidal absorbers to prevent unwanted reflections. In a subsequent step, the terminal was embedded into the rear spoiler and remeasured (see Figure 2b). Eventually, car-integrated measurements were conducted in our automotive antenna measurement facility, the virtual road simulation and test area (VISTA) [14, 15]. The measurement setup consisted of a Skoda Kodiaq car placed on a turntable, with the 3-in-1 antenna mounted in the rear spoiler. The phase center of the measurement arrangement was located at the center of the turntable at a height of 2.3 m above ground. Because the car was

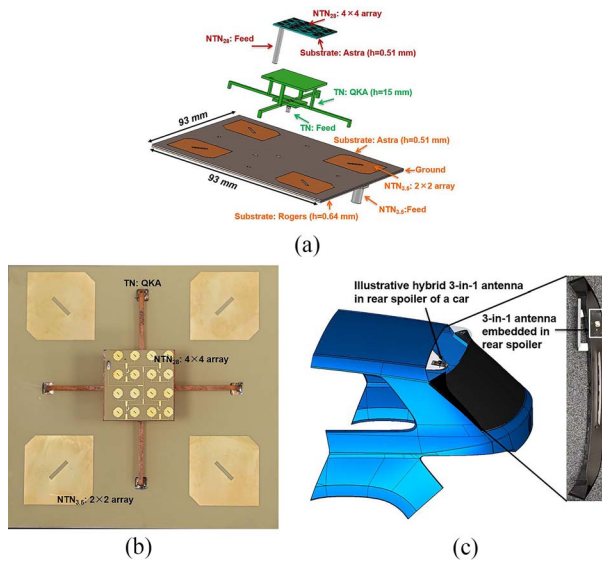


Figure 1. (a) Exploded view of the hybrid 3-in-1 antenna. (b) Photograph of the manufactured version. (c) Photograph of the antenna embedded in the rear spoiler (right) and CAD model of a car with the antenna embedded in the rear spoiler (left).

placed in the middle of the turntable, as depicted in Figure 2c, the antenna mounted in the rear spoiler was offset from the phase center by $(x, y, z) = (-0.33 \text{ m}, 1.94 \text{ m}, -0.10 \text{ m})$. Nearfield measurements of the 3-in-1 antenna were performed at the S-band with the multiprobe antenna arch; the nearfield data were then transformed to far-field using the spherical-wave expansion method [16]. For frequencies above 6 GHz, which exceed the maximum measurable frequency range of the multiprobe system, measurements were conducted using an additional gantry arm equipped with variable antenna measurement payloads [15]. While the nearfield patterns were recorded successfully over the upper hemisphere, these data could not yet be transformed into far-field results due to the lack of the nearfield-to-far-field transformation algorithm at the time of writing.

The results of the measurements are illustrated in Figures 3 to 5. Figure 3a compares the input impedance matching of the simulated QKA across the bands n41 and n78 in the bare state (red-colored curve), the measured data in the bare state (blue), as embedded in spoiler (green), and as integrated into the car (gray). At the frequency bands around $f = 2.6 \text{ GHz}$ and $f = 3.5 \text{ GHz}$, we achieved an input matching of $|S_{11}|^2 < -10 \text{ dB}$ for all versions, each with a nominal operating bandwidth of $\Delta f_{op} \approx 20 \text{ MHz}$. The isolation between the TN antenna and the 2×2 NTN antenna array at 3.5 GHz remained well above 20 dB for the simulated and measured versions (Figure 3b), confirming the benefit of the multilayer design of the NTN array. The realized gain and the total efficiency of the QKA in the embedded state amounted to $G_{TNemb} = 4.7 \text{ dBi}$ (4.4 dBi) and $\eta_{TNemb} = 78\%$ (62%) for the n41 (n78) band. The realized gain of the car-integrated measurement increased to $G_{TNcar} = 6 \text{ dBi}$ (5.6 dBi) in the lower (higher) band. The

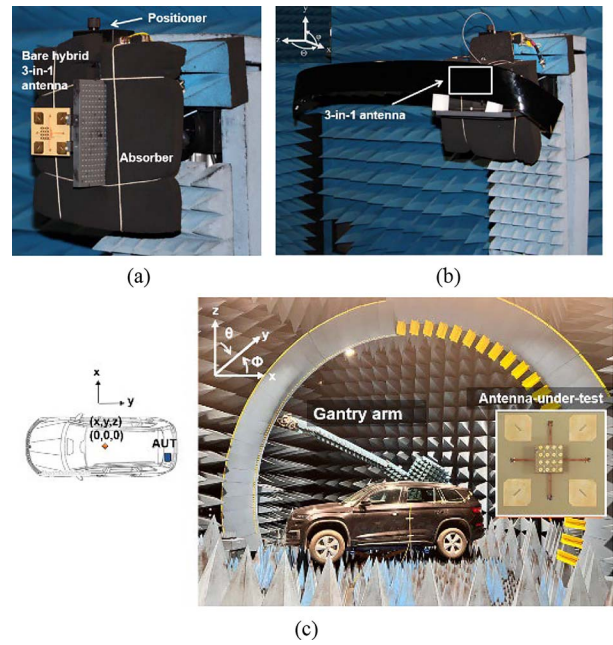


Figure 2. (a) Antenna setup in an anechoic shielded measurement chamber in bare condition, (b) embedded into a rear spoiler, and (c) integrated into a car in the automotive antenna test facility VISTA. [14, 15]

measured vertical cuts at $\Phi = 0^\circ$ revealed a shift from the zenith to $\Theta_0 = 5^\circ$ to 15° at both frequencies; we associate this effect with the hanging coaxial feed of the 28-GHz array. The omnidirectional horizontal patterns of the QKA revealed pronounced ripples for the embedded and car-integrated versions across the two bands. These features indicate a high sensitivity of the QKA to the dielectric embedding in the nearfield and require suitable optimization in the future. However, the polarization purity remained at a high level of $\text{XPD} > 15 \text{ dB}$ for all four versions and at both frequency ranges.

Figure 4 summarizes the results for the 2×2 elements NTN array at $f = 3.5 \text{ GHz}$ with an input matching of $|S_{11}|^2 < -10 \text{ dB}$ across a bandwidth of $\Delta f_{op} \approx 100 \text{ MHz}$ for the simulated and car-integrated measured data. The measurements in the bare and embedded states still reached an acceptable level $|S_{11}|^2 < -6 \text{ dB}$ over a bandwidth of 350 MHz and 120 MHz, respectively. These differences are attributed to additional attenuation by the rear spoiler. The frequency variation of the axial ratio is shown in Figure 4b, confirming the design goal $\text{AR} < 3 \text{ dB}$ around $f = 3.5 \text{ GHz}$ for all data sets. The embedded and car-integrated data display a 3 dB bandwidth of the axial ratio of $B_{AR} \approx 75 \text{ MHz}$. The angular variation of the axial ratio is shown in Figure 4c, exhibiting an elevation range $\Delta\Theta_{NTN} \approx \pm 30^\circ$ with $\text{AR} < 3 \text{ dB}$, except for the embedded state, for which the pattern along co-elevation was tilted to the right. The embedded array offered a realized gain of $G_{NTNemb} = 6.2 \text{ dBi}$, with a total efficiency of $\eta_{NTNemb} = 70\%$. The simulated and measured vertical normalized gain cuts at $\Phi = 0^\circ$ and 90° for the antenna in the bare state agree well, while the measured embedded array showed a distorted pattern

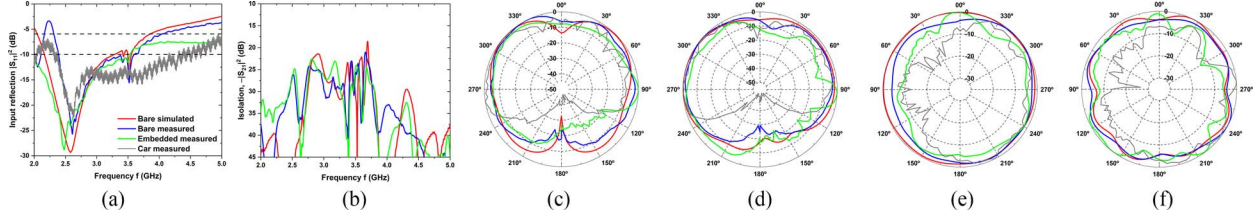


Figure 3. (a) Input reflection $|S_{11}|^2$ for the bare simulated TN (red-colored curve), bare measured (blue), embedded measured (green), and car-integrated measured antenna (gray), (b) isolation $|S_{21}|^2$ between TN and NTN array, (c) vertical cut of normalized realized gain for $\Phi = 0^\circ$ at $f = 2.6$ GHz, (d) at $f = 3.5$ GHz, and (e) horizontal cut of normalized realized gain for $\Theta = 90^\circ$ at $f = 2.6$ GHz and (f) at $f = 3.5$ GHz.

(Figures 4d and 4e). The radiation pattern displayed ripples for the car-integrated data, indicating the influence of the car body, with reduced values for the realized gain ($G_{\text{NTNcar}} = 6.3$ dBi) and total efficiency ($\eta_{\text{NTNcar}} = 25\%$). The car-integrated antenna offered an impedance bandwidth of $B_{\text{NTNcar}} \approx 300$ MHz.

Analogously to the results for the S-band NTN radiator, Figure 5 displays the results for the Ka-band NTN radiator. Compared with the numerical simulations, the minimum $|S_{11}|^2$ values measured for the bare, embedded, and car-integrated versions were recorded at slightly reduced frequencies of 28.6 GHz, 27.5 GHz, and 26 GHz, as shown in Figure 5a. In contrast, the value remained well below -10 dB over the entire n257 band for the car-integrated version. The frequency shift is associated with a change in the dielectric permittivity compared with the initial design values. The frequency variation of the axial ratio is shown in Figure 5b, where $\text{AR} < 3$ dB was achieved around $f = 28$ GHz for all versions, while the measured data appear to be shifted towards higher frequencies compared with the simulation. The 3dB axial ratio bandwidth for the embedded version amounted to $B_{\text{AR}} \approx 1000$ MHz. The measured angular variation of the axial ratio exhibited an elevation range of $\Delta\Theta_{\text{NTN}} = \pm 15^\circ$ with $\text{AR} < 3$ dB for the bare and embedded versions (shown in Figure 5c). The realized gain of the embedded array was $G_{\text{NTNemb}} = 13.1$ dBi compared with the simulated value of $G_{\text{NTNsim}} = 14.6$ dBi, implying a total efficiency of $\eta_{\text{NTNemb}} = 51\%$. This degradation is associated with the current feed design of the 28-GHz array. The radiation patterns are shown in Figures 5d and 5e for the four variants; the car-integrated data refer to nearfield data (gray). The normalized vertical cuts at $\Phi = 0^\circ$ and 90° reveal pronounced ripples for the embedded

versions due to the influence of the dielectric embedding. The embedded antenna offered a 3 dB beamwidth of $\Delta\Theta_{\text{NTN}} = \pm 12^\circ$ and an impedance bandwidth $B_{\text{emb}} > 4.5$ GHz. The vertical cuts at $\Phi = 0^\circ$ and 90° for the car-integrated measurements refer to nearfield data. The Friis transmission equation [17] was adopted to estimate the realized gain. The far-field distance $R = 2D^2/\lambda \approx 1.6$ m for size $D = 93$ mm at $\lambda = 10.7$ mm was satisfied with the measurement distance of 4.5 m. The estimated gain, $G_{\text{NTNcar}} \approx 11$ dBi, serves as an initial value, with further refinement expected via extended nearfield-to-far-field transformation, including translated spherical wave expansion.

5. Conclusions

A compact, dual-band, 3-in-1 user terminal antenna that combines terrestrial and nonterrestrial wireless 5G links with different fields of view has been developed, manufactured, and successfully tested in various antenna measurement facilities. The automotive antenna test range VISTA, with its recent gantry arm extension, enabled measurements of the complete antenna embedded into the rear spoiler and integrated into a passenger sport utility vehicle at the two frequency ranges of interest, around 3.5 GHz and 28 GHz. The measurements revealed promising performance parameters for three different implementation variants, namely bare, embedded into the rear spoiler, and integrated into the car. By comparison with electromagnetic full-wave simulations, we identified ways to optimize antenna performance in terms of decoupling the TN and NTN radiators at 3.5 GHz, reducing symmetry distortion by the feed networks, and mitigating the effects of plastic embedding. These steps bring the design goals for the realized gain values of 10 dBi and 15 dBi for the NTN

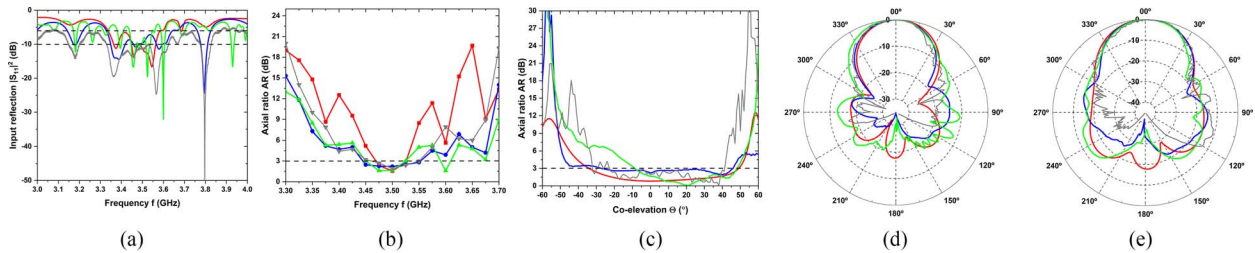


Figure 4. (a) Input reflection $|S_{11}|^2$ for the bare-simulated NTN array at 3.5 GHz (red-colored curve), bare measured (blue), embedded measured (green), and car-integrated measured antenna (gray), (b) axial ratio versus frequency along zenith, $\Theta_0 = 0^\circ$, (c) axial ratio versus co-elevation, (d) vertical cut of the normalized realized gain for $\Phi = 0^\circ$, and (e) for $\Phi = 90^\circ$ (same color coding as in Figure 3).

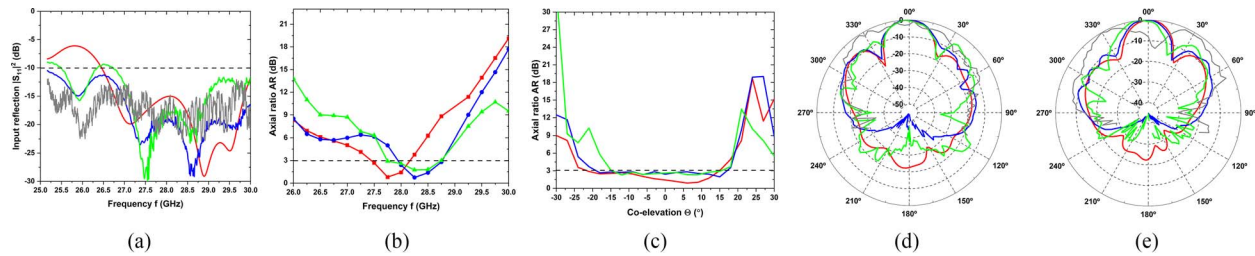


Figure 5. (a) Input reflection coefficients $|S_{11}|^2$ for the bare-simulated (red-colored curve), bare-measured (blue), embedded-measured (green), and car-measured antenna (gray), (b) axial ratio versus frequency along zenith, $\Theta = 0^\circ$, (c) axial ratio versus co-elevation at $f = 28$ GHz, (d) vertical cut of normalized realized gain at $f = 28$ GHz for $\Phi = 0^\circ$, and (e) for $\Phi = 90^\circ$ (same color coding as in Figure 3).

radiators at S-band and Ka-band, respectively, within reach, thus offering promising data rates and transmission latencies for a wide range of relevant use cases in automated and connected driving applications. Future developments may build on these achievements to enhance the wireless coverage in shadowed regions of urban environments or unserved rural areas through complementary NTN links, in addition to terrestrial coverage.

6. Acknowledgments

The authors are grateful for the valuable contributions from Masoumeh Pourjafarian, Michael Huhn, and Dr. Tobias Nowack at ThIMo (TU Ilmenau), from Oliver Wick at BMW AG, and from Mario Nowack at Leipziger Verkehrsbetriebe.

7. References

- G. Fodor, J. Vinogradova, P. Hammarberg, K. K. Nagalapur, Z. T. Qi, et al., "5G New Radio for Automotive, Rail, and Air Transport," *IEEE Communications Magazine*, **59**, 7, July 2021, pp. 22-28.
- U. Tayyab, A. Kumar, H.-P. Petry, M. E. Asghar, and M. A. Hein, "Dual-Band Nested Circularly Polarized Antenna Array for 5G Automotive Satellite Communications," *Applied Sciences*, **13**, 11915, October 2023, pp. 1-15.
- U. Tayyab, M. E. Asghar, and M. A. Hein, "Wide-Band Low-Profile Quadripod Kettle Antenna for Automotive 5G Mobile Communications," ICMIM 2024; 7th IEEE MTT Conference, Boppard, Germany, April 16-17, 2024, pp. 91-94.
- 5G Automotive Association Technical Report "Maximising the Benefit of Future Satellite Communications for Automotive," <https://5gaa.org/maximising-the-benefit-of-future-satellite-communications-for-automotive/> (Accessed 06, June 2025).
- 3GPP TS 38.101-4, "Technical Specifications Group Radio Access Network; NR; User Equipment (UE) Radio Transmission and Reception; Part 4: Performance Requirements," version 17.3.0, https://www.etsi.org/deliver/etsi_ts/138100_138199/13810104/16.03.00_60/ts_13810104v160300p.pdf, January 2022.
- H. Idmouida, K. Minaoui, and Z. Guennoun, "Link Budget Analysis for a 3U Nanosatellite Operating At S-band," 2022 IEEE International Conference on Communication, Networks and Satellite (COMNETSAT), Solo, Indonesia, November 3-5, 2022, pp. 27-32.
- A. R. Dastkhosh, Z. Khan, M. Naseh, and F. Lin, "Link Budget Calculations for K/Ka-band Satellite Mobile Communication Systems," 2022 IEEE MTT-S International Wireless Symposium (IWS), Harbin, China, August 12-15, 2022, pp. 1-3.
- A. Kumar, H.-P. Petry, U. Tayyab, and M. A. Hein, "Link Budget Considerations for Automotive 5G LEO Satellite-Based Communications," 2022 IEEE USNC-URSI Radio Science Meeting, Denver, Colorado, July 10-15, 2022.
- C-V2X, "Use Cases and Service Level Requirements Volume II," <https://5gaa.org/c-v2x-use-cases-and-service-level-requirements-volume-ii/> (Accessed 06, June 2025).
- 3GPP TS 38.104, "Base Station (BS) Radio Transmission and Reception," V18.5.0, https://www.etsi.org/deliver/etsi_ts/138100_138199/138104/18.05.00_60/ts_138104v180500p.pdf, 2024.
- Y. Luo, Q.-X. Chu, and J. Bornemann, "Enhancing Cross-Polarisation Discrimination or Axial Ratio Beamwidth of Diagonally Dual or Circularly Polarised Base Station Antennas by Using Vertical Parasitic Elements," *IET Microwaves, Antennas, and Propagation*, **11**, 9, February 2017, pp. 1190-1196.
- P. I. Deffenbaugh, R. C. Rumpf, and K. H. Church, "Broadband Microwave Frequency Characterization of 3-D Printed Materials," *IEEE Transactions on Components, Packaging and Manufacturing Technology*, **3**, 12, December 2013, pp. 2147-2155.
- Dassault Systems Electromagnetic Simulation Solvers, "CST Studio Suite," <https://www.3ds.com/products/simulia/cst-studio-suite>, 2024.
- M. Hein and F. Saccardi, "Antenna Measurement Challenges and Opportunities," *Reviews of Electromagnetics*, **2**, December 2023, doi: 10.53792/roe/2023/23003.
- C. Andrich, T. F. Nowack, A. Ihlow, S. Giehl, M. Engelhardt, et al., "BIRA: A Spherical Bistatic Reflectivity Measurement System," July 2024, arXiv:2407.13749, doi: 10.48550/arXiv.2407.13749.
- J. E. Hansen, *Spherical Near-Field Antenna Measurements*, London, The Institute of Engineering and Technology, 2008.
- C. A. Balanis, *Antenna Theory: Analysis and Design*. Hoboken, NJ, John Wiley & Sons, 2016.